Statistical description of Collisionless α-particle transport in cases of broken symmetry: from ITER to quasi-toroidally symmetric stellarators

A. Gogoleva, V. Tribaldos and J.M. Reynolds-Barredo

Departamento de Física, Universidad Carlos III de Madrid, 28911 Leganés, Madrid, Spain

E-mail: `Alena.Gogoleva@uc3m.es`

C.D. Beidler

Max-Planck-Institut für Plasmaphysik, 17491 Greifswald, Germany

October 2019

Abstract. The confinement of α-particles is vital for any future fusion reactor. Unfortunately, the inevitable appearance of inhomogeneities in the magnetic field activates the non-collisional transport by virtue of ripple trapping and ripple induced stochastization. While a large and growing body of literature is devoted to the mitigation of these channels of losses for future reactor designs, far too little attention has been paid to characterize the statistical nature of the underlying stochastic process, which is generally assumed to be diffusive. Here the effect of breaking the toroidal symmetry on collisionless α-particle transport is analyzed numerically with a guiding center orbit following code MOCA for several configurations: a perfectly toroidally symmetric ITER-like tokamak and four stellarators with different levels of quasi-toroidal symmetry. Statistical characterization of banana widths, bouncing times and banana center evolution put into question the classical convection/diffusion approach to adequately describe collisionless α-particle transport as the magnetic configuration departs from toroidal symmetry.

1. Introduction

The success of magnetically controlled thermonuclear fusion relies, among other things, on the confinement of α-particles that are not only essential for sustaining fusion conditions, but whose unanticipated losses could compromise the efficiency and, more importantly, put at risk the plasma-facing components. The confinement of α-particles is a complex subject involving the equilibrium magnetic field, plasma and α-particle birth profiles, accompanied by resonant and non-resonant MHD instabilities, turbulence, etc. [1, 2, 3, 4].

Improved particle confinement of reasonably high energetic particles could be achieved by endowing the magnetic field either with a certain type of symmetry, with isodynamicity, which imposes the cross-field drift to vanish at every point, or with the less stringent omnigeneity, that ensures zero time-averaged radial drifts [5, 6, 7]. While for particles that circulate in the plasma with the same direction of motion the absence of net radial drifts is fulfilled *per se*, for trapped or reflected particles that bounce between the reflection points placed at zones of higher field strength rather than being automatic becomes the optimization goal. In any realistic device, due to field corrugations (caused by the discrete number of coils, as in tokamaks and stellarators or by various ripples, as in stellarators) some of these particles are lost. Two main collisionless mechanisms are described relating reflected particle losses with the inhomogeneities of the confining magnetic field: ripple trapping [8], in which particles falling into local ripples result in super-bananas orbits, and ripple induced stochastic processes that make particles change their orbit type close to the bouncing points [9, 10, 11]. While a body of literature was devoted to the mitigation of these losses for future reactor designs [11, 12, 13, 14, 15], not so much attention has been paid to characterize the statistical nature of the stochastic process, which is generally assumed to be *diffusive* [1, 2, 3, 4, 8, 9, 10, 11].

The goal of this work is to study the effect of breaking the toroidal symmetry on the confinement of collisionless trapped α-particles. To this end, several configurations are examined, starting with an ideal, perfectly toroidally symmetric, ITER configuration that will serve as a reference followed by four stellarator configurations with different levels of quasi-toroidal symmetry. The statistical characterization of trapped particle behavior is done numerically with the guiding center orbit following code MOCA [16] supplemented with other techniques to determine trapped particle parameters such as their bouncing times, orbit widths and the radial movement of those orbits. Probability density functions of these basic parameters were obtained as a function of the level of toroidal symmetry. These results are compared with analytical calculations as well as with some newly developed estimations assuming that particles approximately move along the field lines. The *diffusive* nature of the stochastic transport process is examined with different statistical analyses for the five magnetic configurations.

The remainder of the paper is organized as follows. In Section 2 the basic approximations, the guiding center orbit following code and the magnetic configurations are presented along with a new figure of merit to quantify the degree of quasi-toroidal

symmetry. Then the impact of the magnetic configurations together with the initial conditions on the orbit types and the fraction of confined and lost reflected particles are discussed. A new technique is presented at the end of Section 2 allowing to obtain banana centers, widths and bouncing times from particle trajectories the results of which are summarized in Section 3. The fraction of reflected particles and the most probable banana bouncing times obtained from particle trajectories are compared with bounce averaging estimations along field lines, an approximation that is justified based on a new method for calculating connection lengths for arbitrary magnetic configurations. The end of Section 3 is devoted to examine if the statistical properties of α-particle transport agree with the diffusive paradigm. Finally, Section 4 summarizes the results and presents a brief discussion.

2. Configurations and Methods

In trying to establish the basic relation between the confinement of α-particles and the symmetry of the underlying magnetic field three main approximations were made through this work, namely: i) the *small gyroradius ordering*, or drift ordering, ii) neglecting the effect of the electric field and iii) ignoring the collisions with other particle species. The small gyroradius approximation requires $\rho_\alpha/L \sim \omega/\omega_c \sim V_E/v_\alpha << 1$, where ρ_α is the α-particle Larmor radius, L a characteristic plasma spatial scale length (either relevant to profile scales, magnetic field corrugations or banana orbit widths), ω is a characteristic frequency (circulating or bounce α-particles frequency), ω_c is the cyclotron frequency and V_E and v_α are the $\vec{E}\times\vec{B}$ drift and α-particle speeds respectively. Anticipating some of the results of next sections, it is possible to justify that these conditions are fulfilled for α-particles in reactor relevant plasmas. The value of $\rho_\alpha \approx 5$ cm has to be compared with the spatial scales of the orbit widths, $L \sim 0.1 - 0.2\, a \sim 0.3 - 0.6$ m (see Figure 7 left), the magnetic field corrugations $L \sim 1$ m (see Figure 9) and is reasonably valid except perhaps in the pedestal region. The characteristic circulating $\tau_c \sim 2\pi R/v_\alpha \sim 3 - 10\mu s$, bouncing $\tau \sim 10 - 25\mu s$ (Figure 7 right) and collisional slowing-down times $\tau_{slow} \sim 1$ s are also much slower than the cyclotron time. The disparity between v_α and $V_E = \vec{E}\times\vec{B}/B^2$ also justifies neglecting the effect of the radial electric field. A rough estimation of the electric field required for the $V_E \sim E_r/B$ to be comparable with the guiding center drift speed $V_d = mv^2(1+p^2)\vec{B}\times\nabla B/2qB^3 \sim \mathcal{E}_k/qBL$ implies an unrealistically large $E_r \sim \mathcal{E}_k/qL \sim 3.5 \times 10^6/L \sim 10^6 - 10^7$ V/m. Neglecting collisions requires some explanation because despite their initial high speed, α-particles eventually thermalize with the bulk plasma. In reactor conditions α-particle collisional slowing-down time, $\tau_{slow} \sim 1$ s, is faster than the collisional scattering time, $\tau_{scatt} \sim 5$ s [1, 17]. Therefore, depending on the time scales of α-particle confinement it may or may not be justified to include or neglect collisions. Here, to establish a clearer relationship between α-particle confinement and the level of symmetry of the magnetic configuration collisions will be neglected throughout this work.

2.1. Equations of motion

Under these approximations, the motion of α-particles is described by a reduced set of guiding-center equations. One for the velocity of the guiding center,

$$\vec{v}_g = pv\frac{\vec{B}}{B} + \frac{mv^2}{2qB^3}(1+p^2)\,\vec{B}\times\vec{\nabla}B \tag{1}$$

where the two terms account for the fast streaming along the field line and the slow curvature and ∇B drifts across it. The other equation accounts for the variation of the pitch $p = v_\parallel/v$

$$\frac{dp}{dt} = -\frac{v}{2B^2}(1-p^2)\vec{B}\cdot\vec{\nabla}B \tag{2}$$

that arises from the conservation of kinetic energy, $\mathcal{E} = mv^2/2$, and magnetic field moment, $\mu = mv_\perp^2/2B$, which is responsible for the bouncing of some particles at regions with high magnetic fields. Note that neglecting the radial electric field effect and the collisions eliminates the need of an equation for the evolution of the α-particles speed, which is conserved.

When written in Boozer coordinates [18], the equations of motion reduce to 4 ordinary differential equations depending only on the magnetic field strength B and its derivatives with respect to the spatial coordinates (ψ, θ, φ). Where ψ is a normalized toroidal magnetic flux and θ and φ are the poloidal and toroidal angles respectively.

2.2. Configurations

From the infinite number of possible three-dimensional magnetic configurations, two strategies lead to improved particle confinement by endowing the magnetic field either with a certain type of symmetry or with isodynamicity. Here the study will be focused on the effect of breaking the toroidal symmetry of the magnetic field (the most common symmetry). Five configurations will be considered: a purely toroidally symmetry ideal tokamak, that will be used as a reference case, and four stellarators with different levels of quasi-toroidal symmetry (QTS).

For the toroidally symmetric configuration the natural decision was to consider a *ripple-less* ITER [19] tokamak with the following parameters: $B \sim 5.3$ T, $a = 2.67$ m , $R = 6.2$ m and $V \sim 900$ m^3. The four quasi-toroidally symmetric configurations are loosely based on the NCSX [20, 21] stellarator scaled up to have the same ITER nominal magnetic field and volume, which results in a minor and major radius of $a = 2.15$ m and $R = 9.8$ m respectively.

The detailed structure of the magnetic field has been obtained solving the three-dimensional ideal magnetohydrodynamic (MHD) equations with the VMEC code [22]. VMEC finds three-dimensional equilibrium solutions through a variational procedure that minimizes an energy functional with a spectral/finite differences method. VMEC provides the shapes of a given set of nested flux surfaces and the corresponding magnetic field B as a Fourier series constructed in its own internal flux coordinates with a double

periodicity in the poloidal and toroidal angles. The VMEC output is transformed to Boozer flux coordinates (ψ, θ, φ), where the general expression for the magnetic field is also given as a Fourier series for each flux surface:

$$
B^\psi(\varphi, \theta)/B_0 = 1 + \sum_{n=1}^{\infty} \left({}^c B_{0n}^\psi \cos(nN_p\varphi) - {}^s B_{0n}^\psi \sin(nN_p\varphi) \right)
$$
$$
+ \sum_{m=1}^{\infty} \sum_{n=-\infty}^{\infty} \left({}^c B_{mn}^\psi \cos(m\theta - nN_p\varphi) + {}^s B_{mn}^\psi \sin(m\theta - nN_p\varphi) \right) \tag{3}
$$

where N_p is the number of periods of the configuration, $\psi = (r/a)^2$ the normalized toroidal flux, r being the flux surface radius and a the minor radius.

The description of the magnetic field for ITER requires both sine and cosine terms because its D-shape cross-section is not up-and-down symmetric. The expansion for the stellarator only contains cosine terms due to the stellarator symmetry. Despite the full Fourier series has more that 1000 harmonics for each magnetic surface, not all of them are relevant to accurately describe α-particle transport. Here, only modes above a threshold of $|{}^c B_{mn}^\psi|$ or $|{}^s B_{mn}^\psi| > 10^{-4}$ were considered for ITER, which results in including just 7 modes of the expansion (all of them being of the form B_{m0}^ψ). The four quasi-toroidal configurations were generated from the same stellarator equilibrium keeping fixed the few largest modes and adding on top different number of smaller harmonics by setting four thresholds. This method is different to what is done in [23], where configuration's long mean free path transport is modified through the main modes in the quasi-isodynamic stellarator W7-X. The one with higher quasi-toroidal symmetry, called QTS4 throughout this work, was obtained with a larger threshold of $|{}^c B_{mn}^\psi| > 10^{-2}$ and comprises just four ${}^c B_{mn}$ modes; three with $n = 0$ and the smallest one with $n = N_p$, which is responsible for the small toroidal-symmetry breaking. Setting the thresholds to $|{}^c B_{mn}^\psi| > 1/150$ and $1/180$ results in configurations QTS5 and QTS6, described with five and six modes respectively. Finally, the configuration QTS72 is obtained using the same threshold as for ITER ($|{}^c B_{mn}^\psi| > 10^{-4}$) which results in a much broader magnetic field spectrum with seventy-two modes. The ultimate reason for considering these four configurations will become clear in next sections, for the moment it suffices to say that they describe different degrees of departure from quasi-toroidal symmetry. QTS72 configuration looks much more like the configuration one can get with a set of real coils and is further away from the toroidal symmetry. To quantify the degree of quasi-toroidal symmetry of these configurations we followed Alcuson and coworkers and define a figure of merit, σ_{qt}, in a similar way to the one they used for the degree of quasi-poloidal symmetry [24], extending the sums just to the Fourier modes larger than the threshold:

$$
\sigma_{qt}(\psi) = \frac{\sum_{m=1}^{M} |B_{m0}^\psi|}{\sum_{n=1}^{N} |B_{0n}^\psi| + \sum_{m=1}^{M} \sum_{n=-N}^{N} |B_{mn}^\psi|} \leq 1 \tag{4}
$$

Table 1. Values of the quasi-toroidal symmetry ratio σ_{qt} for ITER and the four quasi-toroidal stellarators as a function of radial coordinate.

r/a	ITER	QTS4	QTS5	QTS6	QTS72
0.1	1	0.97	0.96	0.86	0.70
0.5	1	0.94	0.93	0.85	0.62
0.9	1	0.89	0.86	0.83	0.56

where $\sigma_{qt}=1$ stands for perfect quasi-toroidal symmetry, as in a tokamak. Table 1 lists σ_{qt} for the five configurations and three radial positions.

According to the guiding center equations of motion in Boozer coordinates, the radial speed is determined by the variation of the magnetic field with the poloidal and toroidal angles, which for toroidally symmetric and quasi-symmetric configurations approximately reduces to just the poloidal dependence $\partial B/\partial \theta$. The poloidal dependence of the normalized magnetic field, B/B_0, along the field line passing through $\theta = \varphi = 0$ over two poloidal turns around the torus is shown in Figure 1 for three radial positions $r/a = 0.1$, 0.5 and 0.9 of some of the configurations under study. All three configurations display the basic variation due to toroidicity with lower/higher magnetic fields at the outboard/inboard of the equatorial plane and with magnetic field excursions increasing from the axis to the last closed flux surface. The larger poloidal ripple of ITER, due to its tighter aspect ratio, results in larger radial speeds than for the stellarators. However, faster radial drifts do not necessarily mean poorer confinement since particle transport depends on radial speed averages. Here is where the ideal symmetry, $\sigma_{qt} = 1$, comes into play guaranteeing that radial drifts are averaged out. Unfortunately, when the symmetry is broken, $\sigma_{qt} < 1$, there are no such conservation laws that assure the confinement nor guidelines to establish a relation between the level of quasi-symmetry and the average radial drifts. The actual transport of charged particles is the result of ensemble averaging over all possible particle trajectories subjected to all possible realistic physical processes. To show the relation between the magnetic configuration and the confinement in the clearest possible way collisions were not included in this work. Given the number of modes needed to describe the magnetic field, this could only be achieved numerically.

2.3. Numerical Method

The transport properties of the five magnetic configurations are estimated by ensemble averaging α-particle trajectories, that in turn fully depend on the initial conditions in the absence of collisions. An efficient way to calculate guiding center trajectories consists in solving the equations of motion in Boozer coordinates. This was done with the Monte Carlo code MOCA [16]. This code has been thoroughly and successfully benchmarked [25] for an extensive range of stellarator configurations in the past. MOCA is a parallel Fortran code, in which, to speed up the calculations, the magnetic field and its derivatives are pre-stored in a 3D grid $N_\psi \times N_\theta \times N_\varphi$. The high speed of the α-particles,
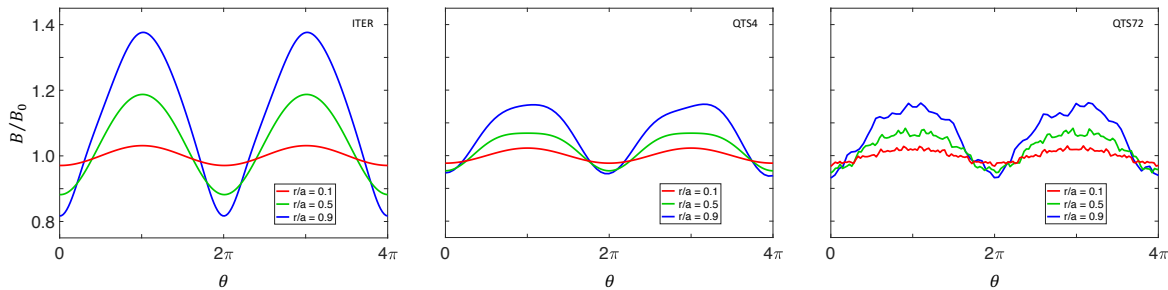
Figure 1. Normalized magnetic field strength along the field line passing through $\theta = \varphi = 0$ as a function of poloidal angle θ for three radial positions $r/a = 0.1$, 0.5 and 0.9 at ITER (left) and the quasi-toroidal stellarators QTS4 and QTS72.

with $v_\alpha = 1.3 \times 10^7$ m/s, and the characteristic spatial magnetic field variation require a short integration time step, $\Delta t \approx 10^{-8}$ s, and a fine grid containing $\sim 100 \times 360 \times 360$ cells per period for numerical accuracy. The computational domain is bounded from one side by the magnetic axis and from the other by the last closed flux surface (particles which cross it are considered lost). A pseudo-Cartesian coordinate system [26] is used to overcome the numerical singularity in the vicinity of the magnetic axis. To describe the initial conditions for the monoenergetic α-particles, it is sufficient to specify their spatial positions and pitch $(\psi_0, \theta_0, \varphi_0, p_0)$.

To obtain statistically significant ensemble averages, the initial conditions have to be representative of the α-particle birth profiles under reactor conditions. Assuming that deuterium and tritium density and temperature profiles are constant on flux surfaces (at least to first order), all particles are initialized radially at half radius, around the mean α-particle birth radius [27], and uniformly distributed over the flux surface. To account for the non homogeneous volume element associated with curvilinear coordinates, particles are initialized uniformly in pitch and randomly in the toroidal and poloidal Boozer angles with a distribution inversely proportional to the Jacobian of the transformation $1/J(\psi, \theta, \varphi) = (B(\psi, \theta, \varphi)/B_0)^2$, thus starting more particles in regions of higher magnetic field strength. Here, the Rejection Method[28] has been used to generate a random sequence in the poloidal (ITER) and poloidal-toroidal (QTS) domains with the prescribed $1/J$ distribution function. The results for ITER were obtained using a set of 65536 particles distributed over 256 poloidal angles with 256 pitch values each, while for the stellarators 262144 particles were used with 4096 initial poloidal-toroidal angles with, again, 64 pitch values each. The simulation time is of the same order of the slowing-down time, which for α-particles in reactor conditions ranges between 0.1-1 s.

Finally, it is worth noting that all the results in this work were checked to be independent of the grid size, the grid interpolation scheme, the integration time step and the number of particles used. Furthermore, the relative energy conservation error has been checked to be below $\sim 10^{-5}\%$ for all particles throughout their lifetimes.
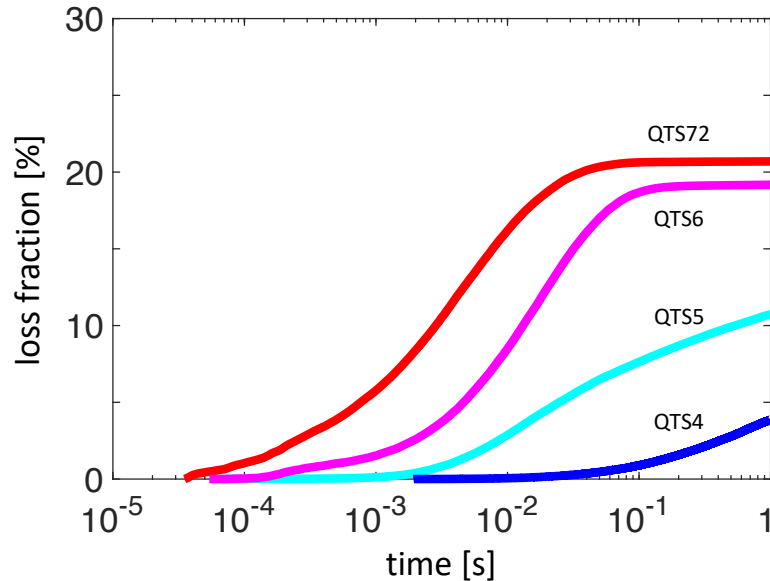
Figure 2. Loss fraction of α-particles over time for the four quasi-toroidal stellarators.

2.4. Impact of the magnetic configuration and the initial conditions on the losses

As a first test of the numerical procedure a set of 65536 α-particles, initially at $r/a = 0.5$ and distributed in poloidal angle and pitch, is followed for 1 s in the idealized and perfectly toroidally symmetric ITER configuration finding that, as expected, none of them get lost. Within this set, there are particles circulating the full plasma with fixed direction of motion, never changing the sign of their pitch and which stayed perfectly confined, the so-called *passing particles* (71%, see Table 2). The other 29% do change the sign of their pitch and are bounded to stay in plasma regions with low magnetic fields, that is why they are called *trapped or reflected particles* and which follow trajectories whose poloidal projection resembles a banana, the so-called *banana orbits*. The fractions of passing and reflected particles presented in Table 2 should not be confused with the effective circulating and trapped particle fractions appearing in neoclassical theory [29, 30, 31] in connection with the dynamics parallel to the magnetic field. In ITER both types have zero average radial drifts, passing particles have it *per se* and reflected particles have it because perfect toroidal symmetry grants well behaved banana orbits. In more realistic ripple tokamaks and quasi-toroidal stellarators trapped particles are expected to experience drifts and precession. This simple picture can easily get blurred when one considers magnetic configurations without symmetry in which new magnetic field ripples give rise to new families of trapped particles with net radial drifts, and even particles that can transit between being passing and being trapped, the so-called *transition particles*. Needless to say, that, even for purely symmetric fields, collisions with background bulk particles may transform passing into trapped particles and vice versa and, moreover, contribute to the net transport by interrupting zero radial

Table 2. Classification and percentage of α-particle types for particles starting at $r/a = 0.5$ for ITER and the four quasi-symmetric stellarators. The simulation time is 1 s.

	Passing	Reflected	
	Confined	Confined	Lost
ITER	71%	29%	0%
QTS4	81%	15%	4%
QTS5	80%	9%	11%
QTS6	79%	2%	19%
QTS72	79%	1%	20%

average drift orbits.

The next step was to repeat the same calculations for the other quasi-symmetric configurations, but now distributing particles in the poloidal and toroidal directions and in pitch ($64 \times 64 \times 64$). We found that despite having a larger fraction of passing particles, $\sim 10\%$ more than ITER (notice the larger ripples in Figure 1), some of the reflected particles get lost. The detailed fractions are given in Table 2. Despite all stellarator configurations have roughly the same fraction of reflected particles, their losses vary from a 4% for QTS4 to a 20% for QTS72. In the absence of collisions, the fate of α-particles only depends on the underlying magnetic field and the initial conditions. Moreover, all lost particles are trapped but not all trapped particles are lost. Figure 2 shows the cumulative loss fraction of α-particles up to $1s$ for the four stellarator configurations. As expected, the higher the symmetry the longer it takes particles to start leaving, the lower the loss rate, the longer it takes to saturate and the smaller the loss fraction.
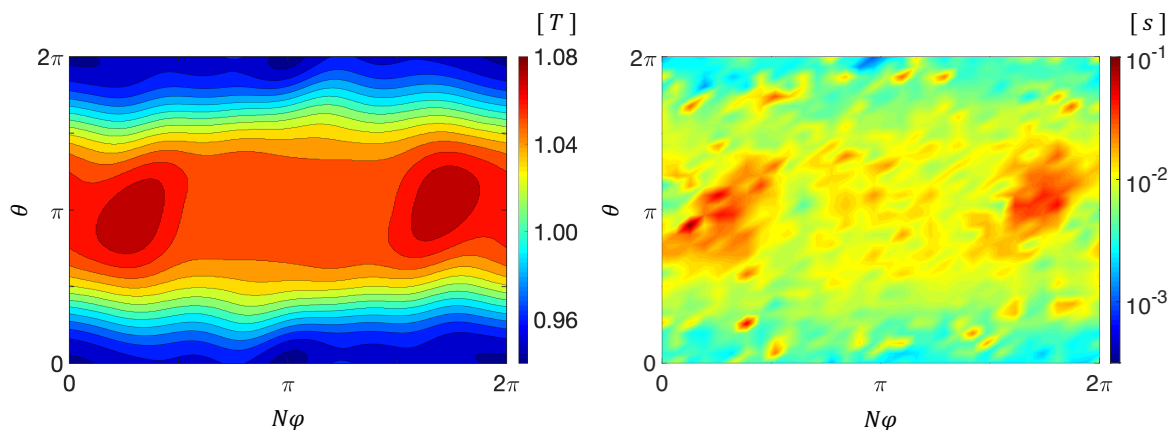

Figure 3. Left: Contours of constant magnetic field strength for one field period. Right: Contours of pitch averaged escaping times as a function of the initial poloidal, θ, and toroidal, φ, positions. Both plots correspond to $r/a = 0.5$ and one period of the QTS72 configuration.

To better understand the relation between α-particle confinement, the magnetic

configuration and the initial conditions in the absence of collisions, Figure 3 (left) shows the contour levels of the magnetic field magnitude at half radius for the QTS72 configuration. The mild toroidal dependence seen is a signature of the approximate toroidal symmetry, where the magnetic field is higher in the inboard ($\theta \sim \pi$) and lower in the outboard ($\theta \sim 0$) sides. The pitch averaged escaping times, calculated with a set of 262144 particles distributed over toroidal, poloidal angles and in pitch, see Figure 3 (right), confirm the weak toroidal dependence and show higher confinement times for particles born in regions of higher magnetic field. Vice versa, particles born in regions with lower magnetic field strength have larger fractions of reflected particles and shorter escaping times.

To further clarify this relation, the escaping times are presented in Figure 4 versus the pitch, averaged over the initial toroidal (left) and poloidal (right) angles. Once again, the results show the feeble toroidal dependence due to the underlying quasi-toroidal symmetry and that only reflected particles with initial pitch $|p| \lesssim 0.35$ are lost. This range of pitch values is consistent with the ripple strength calculated from $\sqrt{1 - B_{min}/B_{max}}$ (see Figure 3 left) for the flux surface under consideration, $r/a = 0.5$. The small pitch asymmetry observed is also compatible with the inward/outward excursion of trapped particles traveling in the co/counter magnetic field direction. The level contours of the toroidal average outline that more/less particles are lost from the outer/inner sides because of the $\sim 1/R$ dependence of the magnetic field with the major radius R. Furthermore, a comparison of both plots shows that the region originating faster losses corresponds to particles with near zero pitch located in the outer part of the stellarator where $|\theta| \lesssim \pi/4$. Particles born in the boundary between the trapped and passing regions (barely-trapped or barely-passing particles) are the ones surviving the longest.
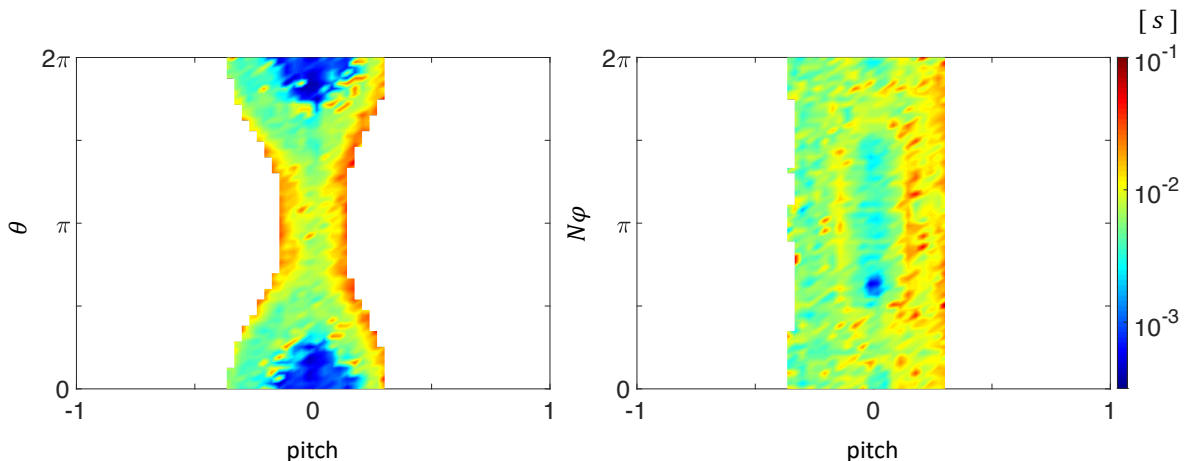

Figure 4. Contours of escaping times as a function of the initial pitch and poloidal angle, θ, averaged over the toroidal angle, φ, (left) and pitch and toroidal angle, φ, averaged over the poloidal angle, θ, (right). Both plots correspond to $r/a = 0.5$ and one period of the QTS72 configuration. White color means no losses.

2.5. Trapped Particle classification

The analysis presented for each configuration shows the relation between where particles were born and their final fate without describing the details about their trajectories. In symmetric configurations, most orbits can be classified into two types: those followed by passing particles, enclosing the magnetic axis and never changing the sign of their pitch, and the ones of reflected particles, bouncing back-and-forth and describing *banana*-shaped trajectories never enclosing the axis. Alongside with these two basic types of orbits, the literature describes many other orbits which are usually special cases of these two. One limiting case is the potato shaped orbits that appears when the banana radial position is comparable to its width. As with bananas, these orbits change the sign of their pitch, but contrary to bananas encircle the axis. Another case is the stagnation orbits, which appears in the phase space boundary between passing and trapped regions where the guiding center speed v_g (see Equation 1) vanishes. In general, these orbits do not encircle the axis nor change the pitch sign, though a general classification, see [32], is out of the scope of this work. The classification is not so simple when the symmetry is broken, even slightly. Along with the passing particles, whose confinement is always guaranteed in the collisionless limit, the lack of symmetry brings new families of orbits, whose radial drifts can lead to the loss of particles or transform trapped into passing particles and vice versa. Therefore, the key element in understanding the confinement of the quasi-symmetric configurations requires characterizing also the new trapped orbits.

The characterization includes the determination of its radial extension, the speed of their radial drift and the frequency of their bouncing. This is done by first selecting those parts of the trajectory of each particle in which it is trapped (this implies that no passing nor stagnation orbits are considered). These sections are then analysed with a newly developed numerical procedure that classifies the orbits into four different types: bananas, ripple trapped, potatoes and others, and estimates, for the bananas, its center, width and bouncing time based on the pitch variation, particularly, the times at which the pitch changes sign.

The classification of trapped orbits uses the poloidal angles at which particles cross the equatorial plane between three consecutive reflection points. Banana orbits, that do not encircle the magnetic axis, are indicated when they only cross the equatorial plane once between reflection points at an angle $\theta = 0$. Potato orbits, that do encircle the magnetic axis, are recognised by the sequence $\theta = 0$ on one orbit side and $\theta = \pi$ on the other, or vice versa. Ripple trapped particles, are distinguished because they do not cross the equatorial plane between consecutive bounces. Obviously, there are orbits that cannot be classified with this method like e.g. those that cross the equatorial plane many times. This is not a severe restriction since reflected orbits are classified for ITER as being $\sim 97.3\%$ bananas, $\sim 0.2\%$ potatoes and $\sim 2.5\%$ unclassified, while for the QTS configurations approximately 90% are bananas, between 2% (QTS4) and 6% (QTS72) ripple trapped, $\sim 1\%$ potatoes and $\sim 5\%$ unidentified. No effort was made in further classifying this 5%, though methods for including more types of orbits are advisable by
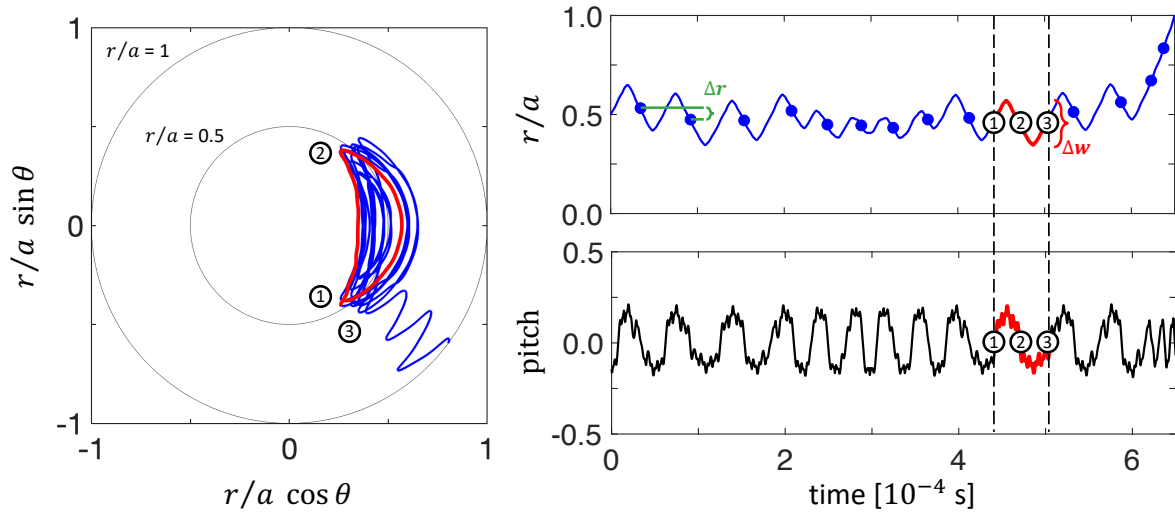
Figure 5. Left: poloidal projection of a trapped α-particle trajectory in Boozer coordinates for the QTS72 configuration from its initial position at $r/a = 0.5$ till its lost at $r/a = 1$. Right: time evolution of the radial position r/a (top) and pitch (bottom) of the same trajectory. The centers of all the banana orbits are indicated by the blue circles (top), $\Delta r \sim 0.06$. The single banana orbit marked in red with reflection points labeled from 1 to 3 has a bouncing time $\tau \sim 30 \, \mu$ s and a normalized orbit width of $\Delta w \sim 0.22$.

using more than three consecutive reflection points and more complex criteria.

As an example of this method, the trajectory of one trapped α-particle for the QTS72 stellarator is shown in Figure 5 in poloidal cross-section (left) together with the time evolution of its radial position (right top) and corresponding pitch (right bottom). The key in the analysis is to notice that every banana orbit is defined by three reflection points, see Figure 5. In the figure one individual banana orbit is drawn in red and labeled with points from 1 to 3. The obvious definition of the bouncing time, τ, is the time that a particle spends between two reflection points. From the mid radial position between two consecutive orbit sides, e.g. r_{12} between r_1 and r_2 or r_{23} between r_2 and r_3 (see Figure 5), it is possible to define the normalized *banana* orbit center as the midpoint, $r_b = (r_{12} + r_{23})/2a$, and the banana width as the difference, $\Delta w = |r_{12} - r_{23}|/a$. Three different procedures were tried to estimate the mid radial positions between two consecutive reflection points using: i) the average radial position, ii) the radial position corresponding to the mid-time and iii) the radial position corresponding to the fastest parallel motion (the maximum absolute pitch). Finally, the second method was used because it is less computationally intensive, though all three procedures give almost the same results.

Every reflected particle trajectory is split into a series of banana orbits and the above method is applied to obtain a *reduced* banana trajectory consisting in the time evolution of its width, Δw, bouncing time, τ, and center, $r_b(t)$, shown as blue dots in the right upper plot of Figure 5. For the orbit of the figure, the bouncing time between points 1-2 and 2-3 is of the order of $\tau \sim 30 \, \mu$ s and the normalized orbit width, indicated

on the right top plot with a bracket, is $\Delta w = 0.22$. This test particle executes twelve banana orbits in approximately 600 μs and slowly drifts radially from $r_b/a = 0.53$ to $r_b/a = 0.6$ before entering in what looks like a toroidal ripple to quickly drift out of the plasma.

In next section this analysis tool is used to statistically estimate the evolution of the banana centers, banana bouncing times and banana widths for the five magnetic configurations with the idea of evaluating convective velocities and diffusion coefficients.

3. Results

In the collisionless limit, there is a deterministic relation between the initial conditions and the destination of every charged particle for a given magnetic configuration. For the *monoenergetic* α-particles, the initial conditions comprise a four dimensional phase-space with the three spatial dimensions and the pitch $(\psi, \theta, \varphi, p)$. Probability density functions of the bounce times and banana widths or the time dependence of the radial distribution of particles are the result of ensemble averaging over the myriad of possible trajectories. Instead of starting directly with the complete problem, we will first examine a simpler case for ITER configuration (where the toroidal angle φ is irrelevant) fixing the initial radial position at ψ_0, thus reducing the dimensionality of the problem from four to two dimensions (θ, p).

3.1. ITER bouncing times and banana widths

With the idea of scanning regions with different well depths, see Figure 1, the methodology described in Section 2.5 was applied to the trajectories of four sets of 4096 α-particles born with initial poloidal angles $\theta = \{0, \pi/4, \pi/2, 3\pi/4\}$, $r/a = 0.5$ ($\psi_0 = 0.25$) and uniformly distributed in pitch between $-0.6 < p < 0.6$ (i.e. in the approximate region where there are trapped particles). The uniform distribution in pitch guarantees that all trapped populations are considered equally. The fraction of reflected particles monotonically decreases with the initial poloidal angle from $\sim 50\%$ at $\theta = 0$, where the magnetic field is the weakest, to $\sim 18\%$ at $\theta = 3\pi/4$, where the magnetic field is stronger. The 1 ms time averaged bounce time $\langle \tau \rangle$ and banana width $\langle \Delta w \rangle$ of each particle are shown in Figure 6 as a function of the initial pitch and poloidal angle. The absence of collisions along with the perfect toroidal symmetry explains why in ITER the curves align nicely depending on its initial poloidal angle. Note that within the guiding center approach no relevant information can be drawn below the Larmor radius ρ_α.

In accordance with [32], the observed dependence of the banana width on the initial poloidal angle and pitch shows that: i) Δw increases with the absolute pitch $|p|$, ii) there is a small pitch asymmetry due to the different inward(co) and outward (counter) banana orbits and to a lesser extent, to the a rotational transform profile, iii) there is a minimum width Δw for reflected particles depending on their initial poloidal position
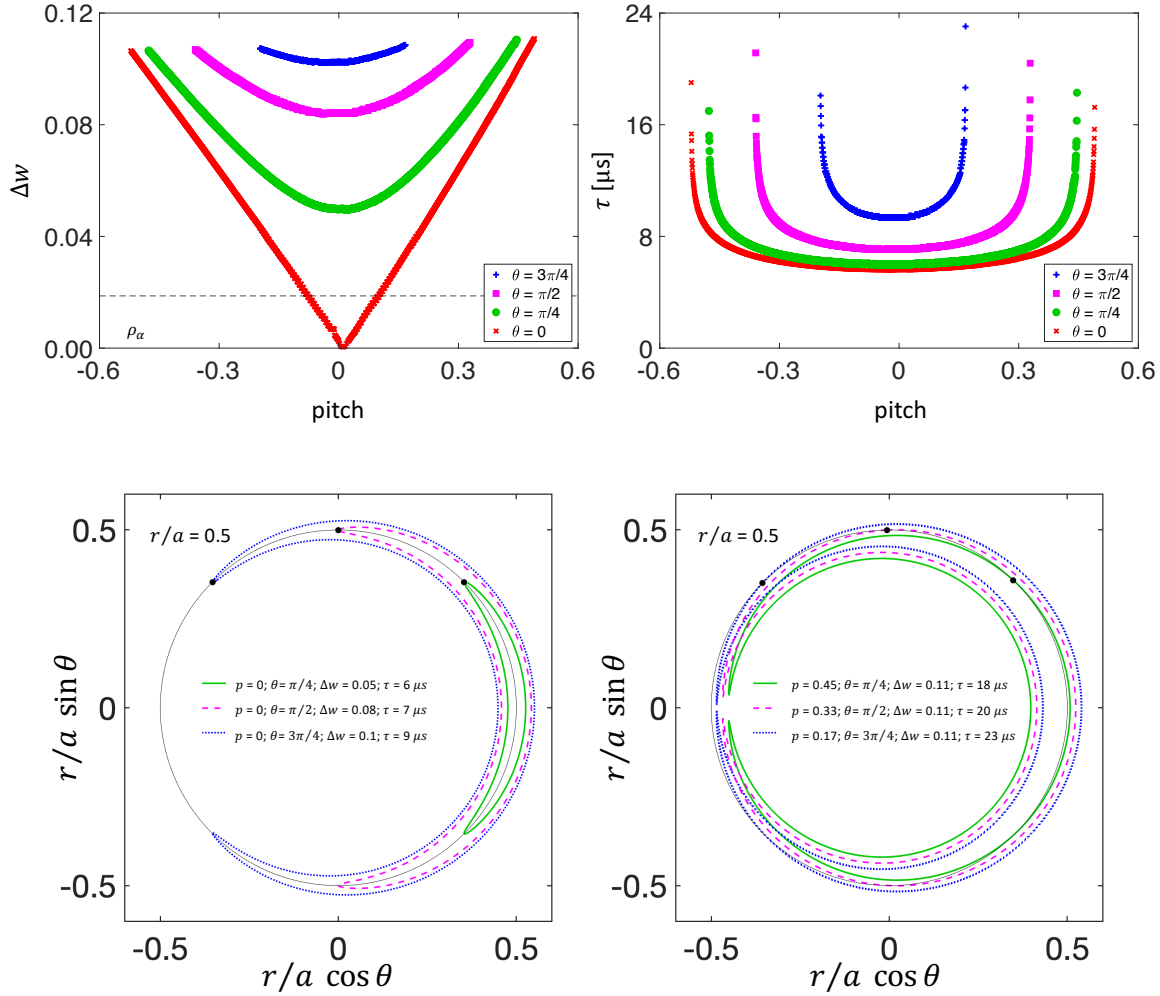
Figure 6. Orbit widths (upper left) and bouncing times (upper right) of reflected α-particles as a function of the initial pitch for ITER configuration. Toroidal projection of banana trajectories for $p = 0$ (lower left) and for initial conditions close to the passing-trapped boundary (lower right). Particles are started from $r/a = 0.5$ and distributed at four poloidal angles $\theta = 0$ (red), $\pi/4$ (green), $\pi/2$ (magenta) and $3\pi/4$ (blue). Each point corresponds to a 1 ms time average of a particle. The α-particle Larmor radius is shown for comparison with a dashed line in the upper left plot.

see the lower left plot of Figure 6 (the higher the field the narrower the pitch range), iv) there is maximum width that does not depend on the initial poloidal position and v) at half radius, the widest bananas extend radially over 10% of the minor radius (~ 30 cm). Regarding the bouncing time it is found that except for the barely trapped particles (the ones initially started at magnetic field B_i and with pitch $|p| \lesssim \sqrt{1 - B_i/B_{max}}$) the bouncing time of most particles is relatively constant, between 6 and 10 μs for our conditions. These values are between 2 to 5 times larger than those traditionally used [33] for the bouncing time, $\tau \approx R/\iota\sqrt{\epsilon}v_\alpha \approx 1.5$ μs and the banana orbit width, $\Delta w \approx \rho_\alpha/\iota a\sqrt{\epsilon} \approx 0.06$, where R is the major radius, $\epsilon = a/R$ the inverse aspect ratio,

ι the rotational transform, ρ_α the Larmor radius and v_α the speed. This is not very severe since these expressions are only valid for ideal tokamaks, vary across different authors up to a numerical coefficient [34, 35, 36], or describe specific particle behaviors or conditions [37, 38, 39].

The fact that bouncing times remain almost constant for a wide range of pitch values (parallel speeds) and initial poloidal positions is especially surprising for particles started at the outboard side because of the disparity of banana widths, compared with the curves corresponding to $\theta = 0$ in both upper plots of Figure 6. This occurs because larger widths are compensated by faster parallel motion (larger absolute pitch) in the same way as the product of the particle parallel speed with the distance along the particle trajectory leads to the conservation of the longitudinal adiabatic invariant $J = \oint v_\parallel \, dl$. Figure 6 also shows that the compensation breaks down for barely trapped particles that spend much longer times close to the bounce points, formally the bouncing time becomes infinite $\tau \to \infty$ [7] since the parallel speed $v_\parallel \to 0$. See the two lower plots of Figure 6. The lack of gyro-phase correlation between consecutive bounces along with the inhomogeneity of the magnetic field is the ultimate reason for the stochastic transport processes described in the literature [8, 9, 10, 11].

We leave for the next section showing the probability density function of orbit widths and bouncing times when particles are distributed over the flux surface for all five configurations.

3.2. Probability density function of bouncing time, orbit width and radial orbit displacement

Using the algorithm presented in Section 2.5, which only applies to reflected particles, the ensemble average orbit widths and bouncing times are calculated for a set of 3.5 MeV α-particles started at $r/a = 0.5$ using the same initial distribution of Section 2.3 (i.e. uniformly distributed in pitch and randomly in the toroidal and poloidal Boozer angles with a distribution inversely proportional to the Jacobian of the transformation). In the case of the toroidally symmetric version of ITER, with a reflected fraction of 30%, this means that from a set of 65536 α-particle trajectories approximately 20,000 are used for the calculation. Since none of these particles get lost, the ensemble average is quite accurate. As for the stellarator configurations, with roughly the same reflected fraction of 20%, from the 262144 α-particle trajectories around 52,000 trajectories are used, though the ensemble average is not as accurate because trajectories are shorter due to the losses (see Figure 1 and Table 1).

To speedup the calculation particles that have not changed their pitch sign during the first 500μs of integration are stopped and eliminated. The precise cutoff was estimated from the escaping time contours of Figures 3 and 4 and the PDF of bouncing times of Figure 7 as a compromise between reducing computer time and taking into account transition particles in the calculation. The probability density functions (PDF) of the normalized banana widths and bouncing times obtained during the lifetime of

the simulated particles are presented in Figure 7 for all five configurations. The PDFs were constructed using the constant bin content method [40] where in all cases each distribution contains more than 10^8 data inputs.
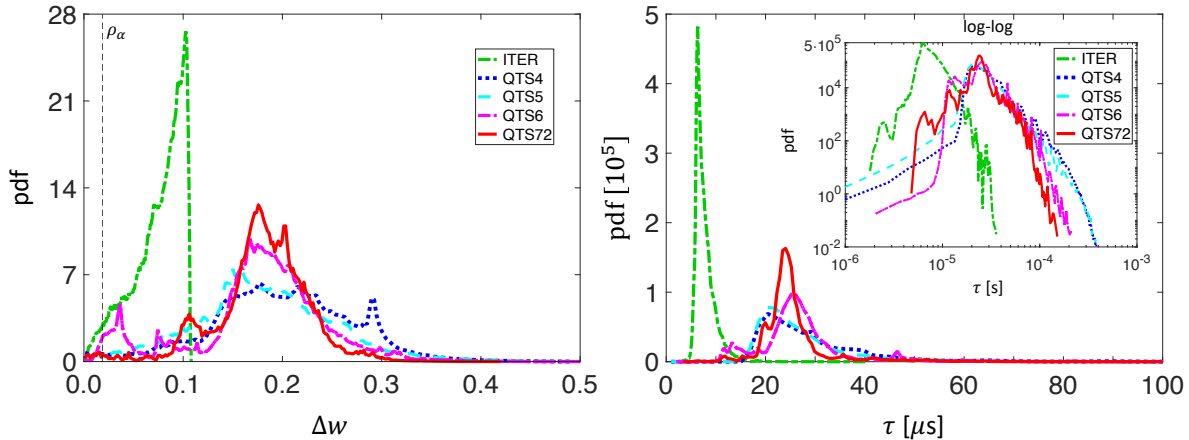

Figure 7. Left: Probability density functions of orbit widths, Δw, of trapped α-particles for ITER and the four quasi-toroidal stellarators. Right: Probability density function of bouncing times, τ, in linear and logarithmic scales.

The probability density function of the normalized orbit widths Δw of reflected α-particles for ITER shows an approximately linear growth that ends abruptly at $\Delta w = 0.11$, in accordance with the negligible number of very small bananas and the maximum orbit width of the left plot in Figure 6. The PDFs of the normalized banana orbit widths for the QTS stellarators are much broader than for ITER, extending up to $\Delta w \sim 0.3$. This clearly indicates the appearance of new wide banana populations and severely puts into question any local approach to transport. There are two main differences compared to ITER: the most probable orbit width is almost twice as large $\Delta w = 0.18$ and that there are other side peaks in the PDF. The extra peaks are probably due to the high order small modular ripples and wider helically trapped bananas.

The right plot of Figure 7 shows the probability density function of the bouncing times τ of trapped α-particles in linear and logarithmic scales. The PDF for ITER has a sharp rise, peaking around $\tau = 8$ μs, followed by a very fast decay (see the log-log scale) ending a bit earlier than $\tau = 16$ μs, which is in perfect agreement with the right plot in Figure 6. The results for the four stellarators are also much broader with the most probable values between $\tau = 20$ and 25 μs. Unfortunately, there is no simple way to compare these results with any analytical expression since little is known about the characteristic scales of motion of trapped particles in stellarators [41, 42, 43] (or even non-ideal tokamaks) and it is unclear to what extent they differ from ideal tokamaks. This is because of the high order field modes, which are virtually impossible to consider analytically and whose effect might be insignificant for trapped particles in general but may be substantial for α-particles. The only available results were carried out numerically for specific configurations considering only the main components of the magnetic field neglecting the rest of the spectrum [32, 44, 45, 46].

The logarithmic scale reveals another difference between the configurations. Whereas an exponential decay in the PDF of ITER starts around $\tau = 10$ μs and lasts till $\tau = 50$ μs, the decay for the stellarators not only starts much later $\tau = 50$ μs but also continues much longer $\tau = 200$ μs. These long tails imply that there are much longer characteristic bouncing times, though their impact into PDFs is of minor relevance - five to nine orders of magnitudes smaller compared to the peak values.

The last piece of information collected from reflected particle trajectories is the evolution of the center of the orbits, $r_b(t)$, and more specifically, the displacements of orbit centers $\Delta r(t_i) = r_b(t_{i+1}) - r_b(t_i)$. In the stochastic view [8, 9, 10, 11] of collisionless transport, it is precisely the *random-walk* displacement of the orbits which gives rise to diffusion. In Figure 8 the probability density function of the orbit center displacements is presented for the five configurations under study. The displacement of ITER trapped orbits is negligible because of its pure toroidal symmetry. On the other hand, the broken symmetry configurations display large and inward/outward asymmetric displacements, which become narrower with higher toroidal symmetry. Note that the most probable orbit widths for these configurations is around $\Delta w \approx 0.2$, and there is a significant probability of having quite large displacements Δr, e.g. the cumulative probabilities $P(|\Delta r| \geq 0.05) \sim 0.25$ and $P(|\Delta r| \geq 0.1) = 0.05$. Moreover, the PDFs clearly show a complex structure with several slopes corresponding to different spatial scales, possibly due to different orbit types, that put into question the local and diffusive nature of the underlying process.
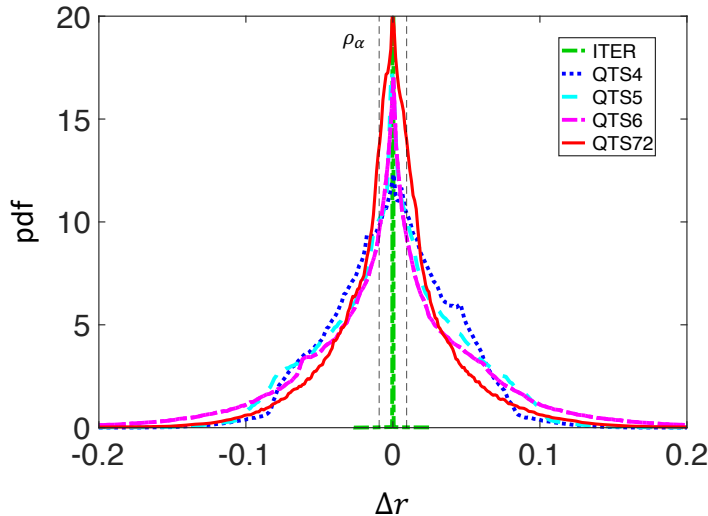

Figure 8. Probability density functions of orbit center displacements Δr (see right upper plot of Figure 5) of trapped α-particles for ITER and the four stellarator configurations.

The behavior of reflected particles, rebounding at regions of high magnetic field, together with the structure of the magnetic field along the field lines, shown in Figure 1, suggest other procedures to characterize the configurations and estimate the bouncing times, which offers the possibility to confirm the results of this Section 3.2.

3.3. Bouncing times and connection lengths

So far, the bouncing time was calculated integrating the guiding center trajectories and explicitly measuring how long does it take particles to reverse their parallel motion. A possible way to validate the results of Section 3.2 is to assume that particles where simply streaming along the field lines. In this approach the time of going along the field line from l_1 to the next consecutive bounce point l_2 would just be $\tau(B) = \int_{l_1}^{l_2} dl/v_\parallel$ where $v_\parallel(l) = v_\alpha \sqrt{1 - B(l)/B}$ and $v_\alpha = 1.3 \times 10^7$ m/s. However, to use this approximation it is necessary to justify that the distance travelled along the field line between bounces is approximately the same as the guiding center trajectory. The fact that the most probable banana widths are $0.1\,a$ (~ 30 cm) for ITER and $0.2\,a$ (~ 60 cm) for the stellarators (see Figure 7) is an encouraging first step, but is not enough until the average distance between bounce points along the field line $\langle |l_2 - l_1| \rangle$ is known. Estimating this distance for an ideal circular tokamak is not very difficult but the same calculation for a D-shape tokamak or a general stellarator has to be done numerically integrating the actual distance along the field line and using the 3D geometric properties of the equilibrium field. Fortunately, this can be done using the toroidal coordinates, (R, Z, φ), of a flux surface ψ, which are given by a series expansion in Boozer coordinates, (θ, φ), similar to Equation 1:

$$R^\psi(\varphi, \theta) = \sum_{m,n \neq 0} {}^cR_{mn}^\psi \cos(m\theta - nN\varphi) + {}^sR_{mn}^\psi \sin(m\theta - nN\varphi) \tag{5}$$

$$Z^\psi(\varphi, \theta) = \sum_{m,n \neq 0} {}^sZ_{mn}^\psi \sin(m\theta - nN\varphi) + {}^cZ_{mn}^\psi \cos(m\theta - nN\varphi) \tag{6}$$

Exploiting that in Boozer coordinates the magnetic field lines are described simply by $\theta = \iota\varphi$, the arc length along the field line and the magnetic field magnitude can be both parametrized as a function the toroidal angle using $dl(\varphi) = \sqrt{(dR/d\varphi)^2 + R^2 + (dZ/d\varphi)^2}d\varphi$ and the expansions of equations 5 and 6. Note that $l(\varphi)$ contains the dependence of the flux surface geometry and the local rotational transform (which is constant in Boozer coordinates) and makes $B(l)$, see Figure 9, different from $B(\theta)$ shown in Figure 1, though they look similar.

If particles were just streaming along field lines, without drifting radially, reflected particles would be bouncing between consecutive points with the same magnetic field. There is a neat way to obtain the characteristic lengths, i.e. the connection lengths, of a configuration for a given flux surface by applying the discrete Fourier transform to $B(l)$, see Figure 10. The main spatial periodicities of the magnetic field, giving rise to the banana orbits, appear as peaks in the Fourier transform, from which the main connection lengths can be calculated for every magnetic configuration and magnetic surface. To accurately capture all the details of the configurations is necessary to follow the field line over a sufficient number of turns around the device. While there is only one significant connection length for ITER of the order of 40 m $\approx 2\pi R$ ($R = 6.2$ m), the stellarator configurations clearly show two of them. The longer connection lengths found
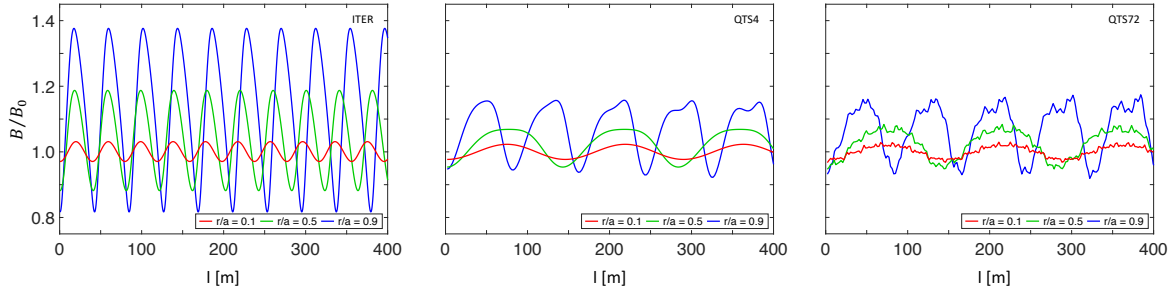
Figure 9. Normalized magnetic field strength along the field line passing through $\theta = \varphi = 0$ as a function of the distance along the field line for three radial positions $r/a = 0.1$, 0.5 and 0.9 at ITER (left) and the quasi-toroidal stellarators QTS4 (center) and QTS72 (right).

for the stellarator configurations, ≈ 140 m, are due to their larger aspect ratio and helical magnetic field components. The largest modes for these stellarators are basically equal because they correspond to the same underlying configuration described by different number of Boozer modes. Moving away from quasi-symmetry, as in QTS72, lead to the appearance of shorter connection lengths with amplitudes larger than 10% of the largest mode. The leading connection lengths obtained using the Fourier transform for ITER, QTS4 and QTS72 are summarized in Table 3 at three radial positions, $r/a = 0.1$, 0.5 and 0.9. The small radial dependence found for ITER is due to the compensation between the field line pitch and the radius, which changes from almost circular close to the axis to a D-shape at outer radii. For the stellarators, the observed smaller connection lengths at outer radius are probably due to the increased importance of the toroidal components, which corresponds to the second most important harmonic ($R = 9.8$ m; $2\pi R \approx 60$ m).
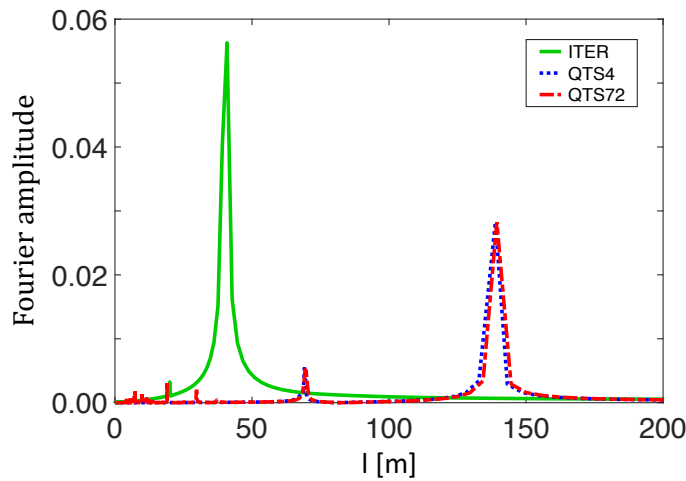

Figure 10. Fourier mode magnitude of the magnetic field along a field line versus $2\pi/k$ at $r/a = 0.5$ for ITER, QTS4 and QTS72.

Table 3. Connection lengths, bouncing times and fraction of reflected particles, f_r, for ITER and the quasi-toroidal stellarators QTS4 and QTS72 at three radial positions. Only connection lengths with Fourier mode amplitudes larger than 10% of the largest mode are shown in decreasing order of magnitude.

	ITER			QTS4			QTS72		
r/a	l [m]	τ [μs]	f_r	l [m]	τ [μs]	f_r	l [m]	τ [μs]	f_r
0.1	41	14	15%	142	56	13%	146 - 71 - 17	11	16%
0.5	41 - 20	6	31%	137 - 69	28	18%	139 - 69 - 16	13	22%
0.9	39 - 20	4	38%	76 - 38	10	25%	76 - 40	8	29%

The smooth radial dependence of the connection lengths together with their magnitude, much larger than that of the most probable radial extension of the orbits (see Figure 7), justifies the assumption that the particles approximately stream along the field lines. Therefore, using the dependence of the magnetic field on the distance along the field line for several turns around the device, it is possible to estimate the average bouncing times for the trapped α-particles using the conservation of energy, $\mathcal{E} = mv^2/2$, and magnetic moment, $\mu = mv_\perp^2/2B$. For a connected region along the field line with magnetic field smaller than a given value $B(l_i < l < l_{i+1}) < B_j$ for $i = 1, ..., N_j$, the time taken between bounces in that well is obtained as the integral $\tau_i(B_j) = \int_{l_i}^{l_{i+1}} dl/v_\parallel$. The procedure is repeated for all connected regions N_j along the field line to get a mean bouncing time for a given magnetic field value $\langle \tau(B_j) \rangle = \sum_i \tau_i(B)/N_j$. Finally, the method is replicated in a regular pitch grid which corresponds to the magnetic field values $B_{min} < B_j < B_{max}$ for $j = 1, ..., N$ to get the mean bouncing time $\tau = \sum_j \langle \tau(B_j) \rangle / N$. A sketch of the procedure is outlined in Figure 11. Likewise, the fraction of reflected particles can be calculated averaging the pitch range over which particles are trapped depending on the depth of the magnetic wells along the field line $\langle f_r \rangle = \int \sqrt{1 - B(l)/B_{max}} dl / \int dl$.

The results of this analysis show a decrease of the bouncing time for increasing radius, independently of the configuration. In case of ITER, τ ranges from 14 μs in the center to 4 μs at the edge. The explanation for the longer bouncing times (56 μs to 10 μs) for the QTS4 stellarator is their longer connection lengths. This effect is compensated by the appearance of shorter connection lengths related to the new ripples in the QTS72 stellarator (12 μs to 8 μs). It is important to notice, that whereas the connection length l is a property of the equilibrium magnetic field, the bouncing time τ is an approximation of the real α-particle motion assuming that particles move along the field lines. The remarkable agreement found in all cases between the bouncing times obtained for $r/a = 0.5$, see Table 3, and the most probable values obtained from the banana orbits of the α-particles, shown in Figure 7, support both the Monte Carlo calculations and the procedure just described along with its approximations. Moreover, the fraction of reflected particles $\langle f_r \rangle$ at $r/a = 0.5$ of Table 3 is also in accordance with
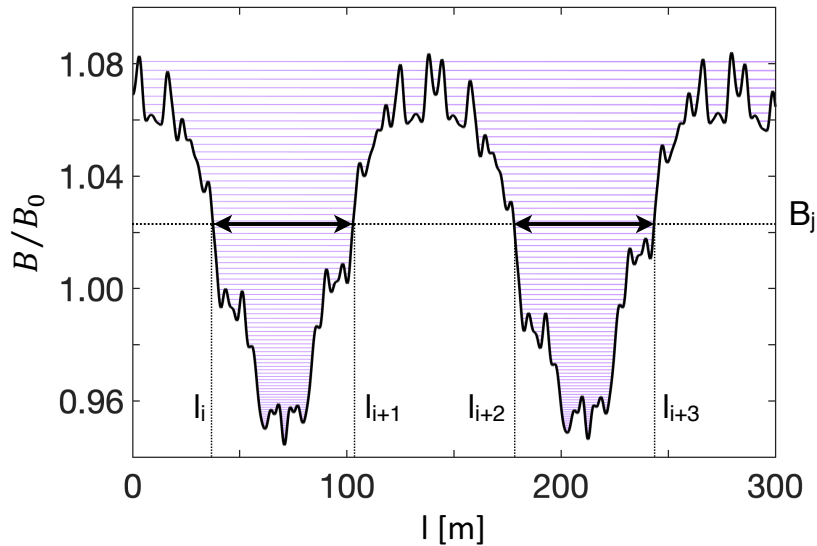
Figure 11. Magnetic field strength versus the length along a field line passing through $\theta = \varphi = 0$ for $r/a = 0.5$ of the QTS72 configuration.

the values of Table 2.

The connection lengths found are between 40 and 150 m, the average banana radial scale length ranges from $0.1a \sim 0.3$ m at ITER to $0.3a \sim 0.6$ m for the four stellarators, which barely supports the local approximation when the minor radii are $a = 2.62$ m and $a = 2.90$ m respectively. On the positive side, both results support the small gyroradius approximation $\rho_\alpha \sim 5$ cm and the gyroaveraged guiding center equations of motion used in this work. The average bouncing times found range from 10 to 30 μs, which are far from α-particle collisional slowing-down $\tau_{slow} \sim 1$ s and scattering $\tau_{scatt} \sim 5$ s times and the expected confinement timescales $\tau_E \sim 5$ s [17], thus partly justifying neglecting collisions in the simulations.

3.4. Transport dynamics

The traditional approach to estimate radial transport consists in assuming that it can be described by a continuous-time stochastic Wiener [47] process, usually referred to as Brownian motion [48] or *random walk*. A convective velocity V and a diffusion coefficient D are traditionally defined from the time evolution of the radial distribution of a set of particles initialized at the same radial position and randomly distributed in the poloidal and toroidal angles and in pitch by using the running moments method [49]. This method, based on [50] estimates both V and D from the slopes of the first and second moments of the radial distribution dependence on time: $\langle \tilde{r}_b \rangle \sim Vt$ and $\langle (\tilde{r}_b - \langle \tilde{r}_b \rangle)^2 \rangle \sim 2Dt$ at very long times, and where $\tilde{r}_b$ is the radial distance travelled by the center of the banana. Thus, in principle one can evaluate the collisionless convection and diffusion due to a magnetic field inhomogeneity from the time dependence of ensemble

averages, $\langle \ \rangle$, of the radial particle distribution.

What is often forgotten is that this method and the underlying assumptions can only be applied when the number of particles is conserved, i.e. when the zero-order moment of the distribution does not depend on time, and for unbound systems (or systems where particles never approach the limits of the system). A condition that only applies when the process is sufficiently slow or when particles do not depart significantly (local *ansatz*) from their initial locations r_0. Unfortunately, the probability density functions of orbit displacements, Δr, and banana width, Δw, shows that this condition is not fulfilled and moreover a considerable fraction of reflected particles can leave the plasma in the quasi-symmetric configurations.

So, the question is to what extent α-particle transport can be described by a Wiener process in toroidally symmetric and quasi-symmetric configurations. The easiest way is to calculate the time dependence of the radial probability density function of α-particle banana orbit centers and check if it has a gaussian shape and/or if it radially drifts. This was done from the simulations of Section 3.2 where the escaping times and radial position of the banana orbit centers were stored at fixed times using the method described in Section 2.5. The escaping time is needed to discard lost reflected particles from the calculation to preserve the conservation of probability.
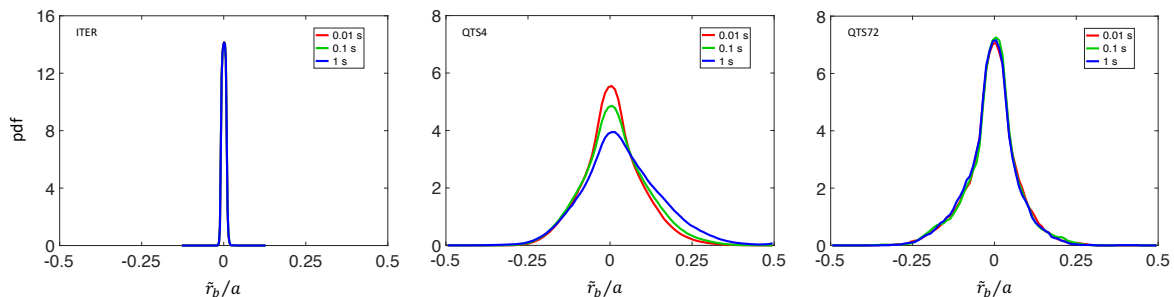

Figure 12. Probability density functions of normalized orbit centers, $\tilde{r}_b/a$, for confined reflected α-particles for ITER (left), QTS4 (center) and QTS72 (right) at $t = 0.01, 0.1$ and 1 s.

The radial probability density function of orbit centers of confined reflected α-particles is presented in Figure 12 for ITER (left), QTS4 (center) and QTS72 (right) configurations at three instants: $t = 0.01, 0.1$ and 1 s. The centers of the banana orbits at ITER, as expected, do not broaden nor drift radially neither inwards nor outwards. The observed width of the distribution, $\Delta r = 0.02a \sim 5$ cm $\approx \rho_\alpha$ serves as an indication of the accuracy of the algorithm determining the banana orbit centers (see Section 2.5). The results for the QTS72 configuration (Figure 12 right) are a bit surprising at first since they resemble those of ITER, although with a much broader radial distribution, which suggests a similarity between the orbit types that survive until 1 s. The difference being that they are a 31% of the particles in ITER and a minuscule 1% in QTS72 (see Table 2). The only confined reflected particles in QTS72 are radially frozen because otherwise they would have been lost. The central plot of

Figure 12 shows a substantial and asymmetric broadening together with a slow outward radial drift for QTS4 configuration. Some particles will be inevitably lost soon after 1s; something that can be anticipated seeing the positive slope of the loss fraction for QTS4 in Figure 2.
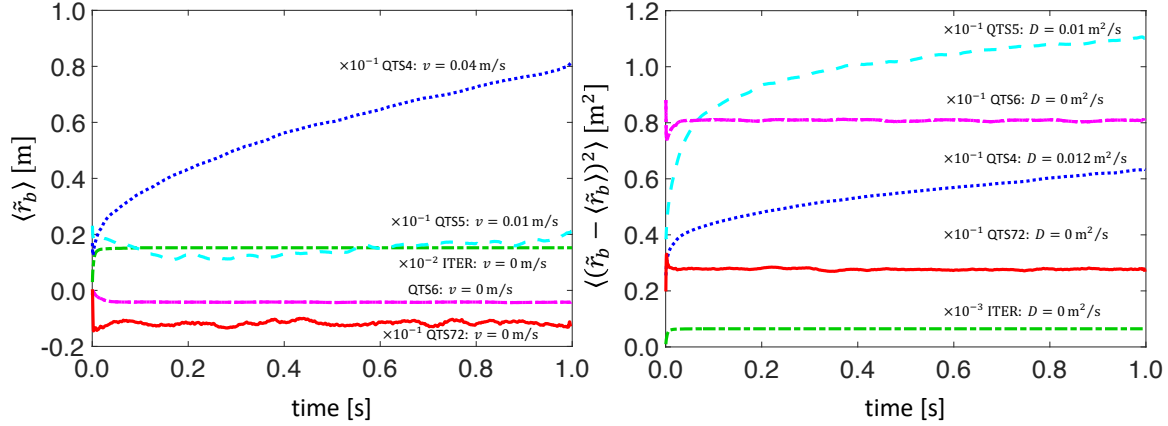

Figure 13. Time dependence of the first (left) and second (right) moments of the probability density function of confined reflected α-particles for ITER and the four QTS configurations.

Applying the running moments method to these radial distributions confirms numerically the visual result of Figure 12. There are almost no convection nor diffusion for ITER, QTS6 and QTS72, $D \sim V \sim 0$, see Figure 13. This is consistent with the collisionless approximation for all ITER reflected particles and the very few QTS6 and QTS72 reflected particles that are not lost in 1 s and also demonstrates that *numerical diffusion* was kept under control in the simulations. For the QTS4 and QTS5 configurations, the values obtained for the convective velocity and the diffusion coefficient from the slope of the first and second moments of the radial distribution are $V = 0.04$ m/s and $D = 0.012$ m^2/s and $V = 0.01$ m/s and $D = 0.01$ m^2/s respectively.

The source of diffusion for the configurations with broken symmetry is the so-called stochastic diffusion, which is due to the magnetic field inhomogeneity [9, 10, 11, 51]. Even for conditions of mildly breaking the toroidal symmetry like in the QTS4 configuration with $\sigma_{qt} \approx 0.9$ at $r/a = 0.9$ and where the fraction of losses is small $< 4\%$, one may be tempted to conclude that these are the transport coefficients of α-particles. However, these values should be put into question when one considers the clear asymmetry of the distribution, its non-gaussian shape and that part of the left side of the distribution remains the same for almost one second, see Figure 12. A remainder that within the 15% of confined reflected particles a certain fraction has no radial drifts, like in ITER and QTS72, though its identification and separation does not seem possible at the moment. Farther away from symmetry, like in the QTS72 configuration with $\sigma_{qt} \approx 0.6$ at $r/a = 0.9$, there is a $\sim 20\%$ of losses and the only confined reflected particles are the ones that do not suffer stochastic diffusion, thus giving the same result

as for ITER. An analysis based on ignoring the warnings and using all trapped particles will result in a time varying PDF normalization (because of the loss of particles) from which no relevant statistical conclusions can be drawn.

Throughout this work, collisions have been intentionally neglected to highlight the link between the magnetic field and the dynamics of α-particles. Collisions mix different types of orbits causing passing particles to become trapped and vice versa, producing diffusion both in real and momentum spaces. For reactor conditions, the characteristic spatial and temporal scales are the banana width and the collisional time. In the case of ITER, where collisionless banana orbits are not drifting radially, see Figure 13, the convective velocity will remain negligible, but the expected diffusion coefficient instead of being zero will depend on the most probable banana width, $\Delta w \sim 0.1$, and the inverse collision time [52], $1/\nu_{coll} \sim 0.1$ s, thus giving $D \sim a^2 \Delta w^2 \nu_{coll} \sim 10^{-2}$ m^2/s. The situation is different for the stellarator configurations since the effect of collisions is barely noticeable below $\sim 10^{-2}$ s [14], i.e. well before losses in QTS4 have started and after most of the QTS72 losses took place, see Figure 2. This time scale is too slow compared to the bouncing times of QTS4, $\tau \sim 20\ \mu$s, and results in a diffusion coefficient, $D \sim a^2 \Delta w^2 / \tau \sim 2 \times 10^4$ m^2/s, inconsistent with the running moments method. As for QTS72, one can expect that some confined orbits are scattered by collisions into regions that further increase the losses, thus supporting the conclusion that the process is not diffusive.

4. Summary and Conclusions

The original goal of this work was to study the effect of breaking the toroidal symmetry of the magnetic field on the transport of collisionless α-particles. To that end, five magnetic configurations were considered with different quasi-toroidal symmetry ratios σ_{qt}: a purely toroidal case with $\sigma_{qt} = 1$ and the parameters of ITER, that serves as a reference, and four stellarator examples, with $\sigma_{qt}(r/a = 0.5)$ ranging from 0.94 (QTS4) to 0.62 (QTS72) derived from a configuration inspired in the NCSX project. The behavior of α-particles was studied with the guiding center orbit following code MOCA.

The analysis of averaging escaping times of an ensemble of particles allowed to estimate the losses of every configuration and its dependence on the birth position. In the symmetric configuration only two types of confined particles, passing and reflected, were found. When toroidal symmetry is broken, apart from passing particles only trapped and transition particles born close to the magnetic field maximum remain confined. Two different methods were used to obtain the fraction of reflected particles f_r, one based on particle trajectories and the other on the magnetic well depth.

A novel algorithm was introduced to define the trapped orbit center, width, and bouncing times based on particle trajectories. It was confirmed that banana width and bouncing times increase as the configuration departs from symmetry. New bouncing times appear as a result of the new field ripples of the quasi-toroidally symmetric

configurations. These results were corroborated by independent numerical procedures for calculating the average bouncing times and connection lengths along the field lines. The statistical analysis of the orbit center displacements, responsible of the stochastic collisionless transport, points to the existence of several entangled spatial scales.

Transport coefficients were estimated by using the calculated most probable banana width and bouncing times ($\Delta w \sim 0.2$ and $\tau \sim 30~\mu$s) and by fitting the time dependence the moments of the radial probability density functions. For the QTS4 configuration, for which both methods can be compared, the first procedure, returns results for the diffusion coefficient $D \sim 2 \times 10^4$ m^2/s which is inconsistent with those obtained by the second method, $D \sim 10^{-2}$ m^2/s.

The results obtained here put into question the classical convection/diffusion approach to adequately describe collisionless trapped α-particles transport as the magnetic configuration departs from toroidal symmetry, a result that can probably be applied to other symmetries. A description based on the use of *fractional transport equations* [53] for collisionless α-particle transport is underway.

5. Acknowledgements

References

[1] W. W. Heidbrink and G. J. Sadler. *Nuclear Fusion*, **34**(4):535–615, 1994.

[2] J. Jacquinot, S. Putvinski, G. Bosia, A. Fukuyama, R. Hemsworth, S. Konovalov, Y. Nagashima, W. M. Nevins, F. Perkins, K. Rasumova, F. Romanelli, K. Tobita, K. Ushigusa, J. W. Van Dam, V. Vdovin, and S. Zweben. ITER Physics Basis. *Nuclear Fusion*, **39**(12):2471–2494, 1999.

[3] A. Fasoli, C. Gormenzano, H. L. Berk, B. Breizman, S. Briguglio, D. S. Darrow, N. Gorelenkov, W. W. Heidbrink, A. Jaun, S. V. Konovalov, R. Nazikian, J.-M. Noterdaeme, S. Sharapov, K. Shinohara, D. Testa, K. Tobita, Y. Todo, G. Vlad, and F. Zonca. *Nuclear Fusion*, 47:S264–S284, 2007.

[4] V. Yavorskij, L. G. Eriksson, V. Kiptily, K. Schoepf, and S. E. Sharapov. *Journal of Fusion Energy*, **34**(4):774–784, 2015.

[5] D. Palumbo. *Il Nuovo Cimento B Series*, 53:507–511, 1968.

[6] L. S. Hall and B. McNamara. *Physics of Fluids B*, 18(5):552–565, 1975.

[7] P. Helander. *Reports on Progress in Physics*, **77**(8):087001, 2014.

[8] R. J. Goldston and H. H. Towner. *Journal Plasma Physics*, **26**(2):283–307, 1981.

[9] R. J. Goldston, R. B. White, and A. H. Boozer. *Physical Review Letters*, **47**(9):647–649, 1981.

[10] R. B. White and H. E. Mynick. *Physics of Fluids B*, **1**(5):980–982, 1989.

[11] C. D. Beidler, Ya. I. Kolesnichenko, V. S. Marchenko, I. N. Sidorenko, and H. Wobig. *Physics of Plasmas*, **8**(6):2731–2738, 2001.

[12] S. V. Konovalov, E. Lamzin, K. Tobita, and Yu. Gribov. In *28th EPS Conference on Contr. Fusion and Plasma Phys., Funchal, 18-24 June, ECA Vol. 25A*, pages 613–616, 2001.

[13] M. Drevlak, J. Geiger, P. Helander, and Y. Turkin. *Nuclear Fusion*, **54**(7):073002, 2014.

[14] S. A. Henneberg, M. Drevlak, C. Nührenberg, C. D. Beidler, Y. Turkin, J. Loizu, and P. Helander. *Nuclear Fusion*, **59**(2):026014, 2018.

[15] M. D. J. Cole, R. Hager, T. Moritaka, S. Lazerson, R. Kleiber, S. Ku, and C. S. Chang. *Physics of Plasmas*, **26**(3):032506, 2019.

[16] V. Tribaldos. *Physics of Plasmas*, **8**(4):1229–1239, 2001.

[17] R. V. Budny. *Nuclear Fusion*, **42**(12):1382–1392, 2002.

[18] A. H. Boozer and G. Kuo-Petravic. *Physics of Fluids*, **24**(5):851–859, 1981.

[19] J. M. Reynolds-Barredo, V. Tribaldos, A. Loarte, A. R. Polevoi, M. Hosokawa, and R. Sánchez. *Submitted for publication*, 2019.

[20] M. C. Zarnstorff, L. A. Berry, A. Brooks, E. Fredrickson, G-Y. Fu, S. Hirshman, S. Hudson, L-P. Ku, E. Lazarus, D. Mikkelsen, D. Monticello, G. H. Neilson, N. Pomphrey, A. Reiman, D. Spong, D. Strickler, A. Boozer, W. A. Cooper, R. Goldston, R. Hatcher, M. Isaev, C. Kessel, J. Lewandowski, J. F. Lyon, P. Merkel, H. Mynick, B. E. Nelson, C. Nuehrenberg, M. Redi, W. Reiersen, P. Rutherford, R. Sanchez, J. Schmidt, and R. B. White. *Plasma Physics and Controlled Fusion*, **43**(12A):A237–A249, 2001.

[21] B. E. Nelson, L. A. Berry, A. B. Brooks, M. J. Cole, J. C. Chrzanowski, H. M. Fan, P. J. Fogarty, P. L. Goranson, P. J. Heitzenroeder, S. P. Hirshman, G. H. Jones, J. F. Lyon, G. H. Neilson, W. T. Reiersen, D. J. Strickler, and D. E. Williamson. *Fusion Engineering and Design*, **66-68**:205–210, 2003.

[22] S. P. Hirshman, W. I. van RIJ, and P. Merkel. *Computer Physics Communications*, **43**(1):143–155, 1986.

[23] J. Geiger, C. D. Beidler, Y. Feng, H. Maaßberg, N. B. Maruschenko, and Y. Turkin. *Plasma Phys. Control. Fusion*, 57(014004):1–11, 2015.

[24] J. A. Alcuson, J. M. Reynolds-Barredo, A. Bustos, R. Sanchez, V. Tribaldos, P. Xanthopoulos, T. Goerler, and D. E. Newman. *Physics of Plasmas*, **23**(10):102308, 2016.

[25] C. D. Beidler, K. Allmaier, M. Yu. Isaev, S. V. Kasilov, W. Kernbichler, G. O. Leitold, H. Maaßberg, D. R. Mikkelsen, S. Murakami, M. Schmidt, D. A. Spong, V. Tribaldos, and A. Wakasa. *Nuclear Fusion*, **51**(7):076001, 2011.

[26] G. Kuo-Petravic. *Journal of Computational Physics*, **52**(1):209–213, 1983.

[27] S. Äkäslompolo, T. Kurki-Suonio, O. Asunta, M. Cavinato, M. Gagliardi, E. Hirvijoki, G. Saibene, S. Sipilä, A. Snicker, K. Särkimäki, and J. Varje. *Nuclear Fusion*, **55**(9):093010, 2015.

[28] W. H. Press, S. A. Teukolsky, W. T. Vetterling, and B. P. Flannery. *Numerical Recipes - The Art of Scientific Computing*. Cambridge University Press, second edition, 1994.

[29] A. A. Galeev and R. Z. Sagdeev. *Sov. Phys. JETP*, 26(1):233–240, 1968.

[30] M. N. Rosenbluth, R. D. Hazeltine, and F. L. Hinton. *Physics of Fluids*, 15(1):116–140, 1972.

[31] S. P. Hirshman and D. J. Sigmar. *Nuclear Fusion*, 21(9):1079–1201, 1981.

[32] J. Egedal. *Nuclear Fusion*, **40**(9):1597–1610, 2000.

[33] B. B. Kadomtsev and O. P. Pogutse. *Sov. Phys. JETP*, **24**(6):1172–1179, 1967.

[34] B. B. Kadomtsev, O. P. Pogutse, and I. V. Kurchatov. *Nuclear Fusion*, **11**(1):67–92, 1971.

[35] T. E. Stringer. *Plasma Physics*, **16**(7):651–659, 1974.

[36] A. H. Boozer. *Physics of Fluids*, **23**(11):2283–2290, 1980.

[37] F. Porcelli, L. G. Eriksson, and I. Furno. *Physics Letters A*, **216**(6):289–295, 1996.

[38] A.J. Brizard. *Physics of Plasmas*, **18**(2):022508, 2011.

[39] K. C. Shaing, M. Schlutt, and A. L. Lai. *Physics of Plasmas*, **23**(2):022508, 2016.

[40] R. Sánchez and D. Newman. *A Primer on Complex Systems - With Applications to Astrophysical*

and Laboratory Plasmas. Springer Netherlands, 2018.

[41] V. P. Nagornyj and V. A. Yavorskij. *Sov. J. Plasma Phys.*, **15**(5):534–545, 1989.

[42] M. S. Smirnova. *Nuclear Fusion*, **36**(11):1455–1476, 1996.

[43] M. Wakatani. *Stellarator and Heliotron Devices.* Oxford University Press, 1998.

[44] J. A. Rome. *Nuclear Fusion*, **35**(2):195–206, 1995.

[45] R. Farengo, H. E. Ferrari, M. C. Firpo, P. L. Garcia-Martinez, and A. F. Lifschitz. *Plasma Physics and Controlled Fusion*, **54**(2):025007, 2012.

[46] M. Khan, A. Zafar, and M. Kamran. *Journal of Fusion Energy*, **34**(2):298–304, 2015.

[47] N. Wiener. *Journal of Mathematics and Physics*, **2**(1-4):131–174, 1923.

[48] M. Kac. *Proceedings of the National Academy of Sciences*, **35**(5):252–257, 1949.

[49] R. Balescu. *Aspects of Anomalous Transport in Plasmas.* CRC Press, 2005.

[50] A. Einstein. *Annalen der Physik*, 322(8):549–560, 1905.

[51] P. N. Yushmanov, J. R. Cary, and S. G. Shasharina. *Nuclear Fusion*, **33**(9):1293–1303, 1993.

[52] D. L. Book. NRL Plasma Formulary. Naval research Laboratory, Washington, DC, 1990.

[53] R. Sánchez and D. E. Newman. *Plasma Phys. Control. Fusion*, 57(123002):1–56, 2015.